Bridge Deck and Guardrail Anchorage Detailing for Sustainable Construction

Hossein Azimi, A.M.ASCE[1]; Khaled Sennah, M.ASCE[2]; Mahmoud Sayed-Ahmed[3]; Navid Nikravan[4]; Jacob Louie[5]; Adam Hassaan[6]; and Nabil Al-Bayati[7]

Abstract: This paper investigates the use of glass fiber reinforced polymer (GFRP) bar bents as stirrups at the joint between the steel posts of a bridge guardrail system with a deck slab cantilever. In addition, GFRP bars with headed ends are used for better anchorage at the postdeck slab joint. Four full-scale cantilever post specimens were erected and tested to collapse. Two specimens were reinforced with steel bars as control specimens, whereas the other two specimens were reinforced with GFRP straight bars, bent bars, and headed bars at applicable locations. Similar failure modes were observed in all specimens because of curb external side face breakout. Failure occurred in unconfined concrete cover because of significant compressive and frictional shear stresses and also torsional effects, resulting in concrete spalling at the side face of the cantilever at the bottom of the posts. Although it is recommended to consider larger edge distance of the post to prevent premature failure in the unconfined concrete cover, the obtained experimental capacity of the postcurb region was concluded to be sufficient to resist design loads. To calculate the share of the design lateral loads received by each post, a linear finite-element analysis (FEA) and a simplified FEA were used. The analysis showed that the share of each post decreases with decrease in spacing between posts. **DOI: 10.1061/(ASCE)BE.1943-5592.0000613.**

Author keywords: Steel guardrail system; Bridge overhang; Steel post; Deck joint capacity; Glass fiber reinforced polymer (GFRP) bents; GFRP headed bars; Experiment; Finite-element analysis.

Introduction

Fiber-reinforced polymers (FRPs), as noncorrodible materials, are considered an excellent alternative to reinforcing steel bars in bridge decks to overcome steel corrosion-related problems. FRP materials possess the necessary property of high tensile strength compared with reinforcing steel bars, introducing them as a suitable structural reinforcement for concrete. The application of glass FRP (GFRP) bars in concrete bridge decks is now adopted in structural codes [Canadian Standards Association (CSA) 2006a, AASHTO 2009]. Apart from the deck slab, the application of GFRP bars in bridge railing system has been studied. El-Gamal et al. (2007) conducted pendulum impact testing on performance level 2 and 3 (PL-2 and PL-3) barrier walls reinforced with GFRP bars. Application of GFRP bars in bridge open post railing was studied by Matta and Nanni (2009) using monotonic tests, and modes of failure were studied both experimentally and analytically. In addition, the application of headed GFRP bars in bridge barriers was studied by Sennah et al. (2011a) with crash testing. Ahmed et al. (2013) investigated the ultimate load-carrying capacity and deformation of prototype steel post-and-beam barrier systems with the curb and adjoining bridge deck reinforced with GFRP bars in lieu of steel bars. Experimental evidence was gained through quasi-static load tests that the lateral resistance of the GFRP-RC curb is similar to that of steel-reinforced counterparts. However, the GFRP-RC systems undergo greater postcracking deformations compared with steel RC ones because of the smaller elastic modulus of the GFRP reinforcement.

Application of a steel guardrail system comprising galvanized steel post and rails is still an interesting method for railing systems in bridges because of the ease of rehabilitation or replacement of damaged ones after vehicle impact. Although such guardrails may not be extensively prone to corrosion, the steel reinforcement in the concrete deck is affected particularly from the application of deicing salts in winter. Therefore, a galvanized railing system with deck slab reinforced with GFRP bars could be a much more durable system. In this paper, steel bars are replaced with GFRP bars with ribbed surface, and the steel post is tested to failure under lateral load to investigate the load-carrying capacity of the post–curb junction. The guardrail's post is connected to the deck overhang with steel anchor bolts. The anchor bolts and the base plate transfer the lateral load to the concrete deck. The modes of failure in anchor bolts depend on the type of the applied force, configurations of bolts, and their distance from the concrete edge. They may fail in tension, shear, or interaction between tension and shear [Eligehausen et al. 2006; American Concrete Institute (ACI) 2011; Canadian Standards Association (CSA) 2004]. When the steel post is subjected to lateral load, the anchor bolts are generally under shear and tension.

[1]Adjunct member and FQRNT Post-Doctoral Fellow, Civil Engineering Dept., Ryerson Univ., 350 Victoria St., Toronto, ON, Canada M5B 2K3 (corresponding author). E-mail: hossein.azimi@ryerson.ca

[2]Professor and Chair, Civil Engineering Dept., Ryerson Univ., 350 Victoria St., Toronto, ON, Canada M5B 2K3.

[3]Ph.D. Student, Civil Engineering Dept., Ryerson Univ., Toronto, ON, Canada M5B 2K3.

[4]Ph.D. Student, Civil Engineering Dept., Ryerson Univ., Toronto, ON, Canada M5B 2K3.

[5]Undergraduate Student, Civil Engineering Dept., Ryerson Univ., Toronto, ON, Canada M5B 2K3.

[6]Undergraduate Student, Civil Engineering Dept., Ryerson Univ., Toronto, ON, Canada M5B 2K3.

[7]Researcher, Civil Engineering Dept., Ryerson Univ., Toronto, ON, Canada M5B 2K3.

Note. This manuscript was submitted on August 6, 2013; approved on February 18, 2014; published online on March 20, 2014. Discussion period open until August 20, 2014; separate discussions must be submitted for individual papers. This paper is part of the ***Journal of Bridge Engineering***, © ASCE, ISSN 1084-0702/04014039(12)/$25.00.

Anchor bolt failure modes in tension are steel rupture,; concrete cone breakout; local concrete side blow-out, pull-out, or pull-through; and concrete splitting (Eligehausen et al. 2006). Steel rupture occurs if the anchor bolt itself fails, and concrete cone breakout may happen if the embedment depth of the anchor bolt is small. If a headed anchor stud is under tension and located close to the concrete edge, the local concrete side blow-out can be observed. Pull-out failure occurs by a combination of sliding of the anchor bolt through the hole and concrete failure on top of the hole. Concrete splitting failure is also feasible if the size of the specimen is small or the tension bolts are located close to the concrete edge.

Anchor bolt failure modes in shear are steel failure, concrete edge failure (breakout), and concrete pry-out. Concrete edge failure depends on the arrangement of anchor bolts and the edge distance (CSA 2004). Concrete pry-out failure occurs if the anchor bolt is sufficiently far from the concrete edge and the depth of the anchor bolt is small. At this type of failure, the concrete is sliced out at the same side that shear force is applied. Fig. 1 shows a schematic diagram of concrete breakout at edge because of shear loading (ACI 2011).

In the cases that shear and tension are present at the anchor bolts, the bolts can be examined by the interaction formula (or diagram) provided by the ACI (2011) or the CSA (2004). The capacity of each bolt in tension and shear is calculated separately and then used in the interaction formula. However, in the cases that moment is also present, base plate yielding may also occur. Another mode of failure is the punching shear at the edge of the slab overhang because of the resultant compression force applied at the base plate as shown in Fig. 2(a) (AASHTO 2012). AASHTO load and resistance factor design (LRFD) specifies the following formulas to obtain the punching shear capacity, V_r:

$$V_r = \phi V_n \tag{1a}$$

$$V_n = v_c \left[W_b + h + 2\left(E + \frac{B}{2} + \frac{h}{2} \right) \right] h \tag{1b}$$

$$v_c = \left(0.0633 + \frac{0.1265}{\beta_c} \right) \sqrt{f_c'} \le 0.1265 \sqrt{f_c'} \tag{1c}$$

in which $(B/2) + (h/2)$ and $\beta_c = W_b/d_b$, where W_b = width of base plate; h = slab depth; E = distance from edge of slab to centroid of compressive strength resultant in post; B = distance between centroids of tensile and compressive strength resultant in post; f_c' = concrete compressive strength; and d_b = distance from the outer edge of the base plate to innermost row of bolts. In addition, the resistance factor, ϕ, = 1.0 as specified by AASHTO (2012). In this paper, the lateral capacity of steel guardrail posts with PL-2 attached to bridge cantilever overhang slab is studied. Four slabs are considered, two identical GFRP-reinforced specimens and two identical steel-reinforced counterparts as control specimens. Experimental results and modes of failure are examined and discussed in detail, and proper recommendations are drawn.

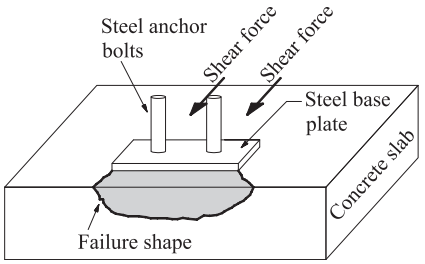

Fig. 1. Schematic diagram of concrete breakout at edge because of shear loading (data from American Concrete Institute 2011)

Experimental Program

Properties of GFRP Bars

In case of bridge deck slab and cantilevers, GFRP bars with headed ends are used as straight bars with an end head to reduce their development length, thus avoiding the use of hooks. The head is made of a thermosetting polymeric concrete with a compressive strength far greater than that of normal-grade concrete. It is cast onto the end of the straight bar and hardened at elevated temperatures. The concrete mix of the head contains an alkali-resistant vinyl ester resin, the same material used in the straight bars, and a mixture of fine aggregates. The maximum outer diameter of the head is 2.5 times the diameter of the bar. The head of the 16-mm bar is 100 mm long. It begins with a wide disk that transfers a large portion of the load from the bar into the concrete. Beyond this disk, the head tapers in five steps to the outer diameter of the blank bar as shown in Fig. 3(a).

The Canadian Highway Bridge Design Code (CHBDC) (CSA 2006a) allows the use of GFRP bent bars in bridges. GFRP bent bars made from straight bars are much weaker than straight bars, because of the redirection and associated rearrangement of the fibers in the bents. As a result, the number of GFRP bent bars may need to be increased and even doubled at such locations where bar bents are required. To reduce the effect of the bent on tensile stresses, a newly developed GFRP bent bar (Schoeck Canada Inc. 2013) was manufactured by bending a specially made polypropylene conduit pipe into the desired shape after filling it with glass fibers and a vinyl ester epoxy resin in liquid condition. These raw bars are then thermally cured. This procedure allows for high fiber content and a nearly parallel alignment of the fibers in the bent portion of the bars, resulting in high strength and modulus of elasticity very close to those of straight GFRP bars. The corrugated shape of the conduct pipe ensures the bond with concrete. A view of the bent bar is shown in Fig. 3(b), and a slice of the bent bar is depicted in Fig. 3(c). This developed GFRP bent was proposed to be used in one of the new bridges in Ontario. These GFRP bents are used in the current research to strengthen the deck-slab curb for torsional-shear effects. The

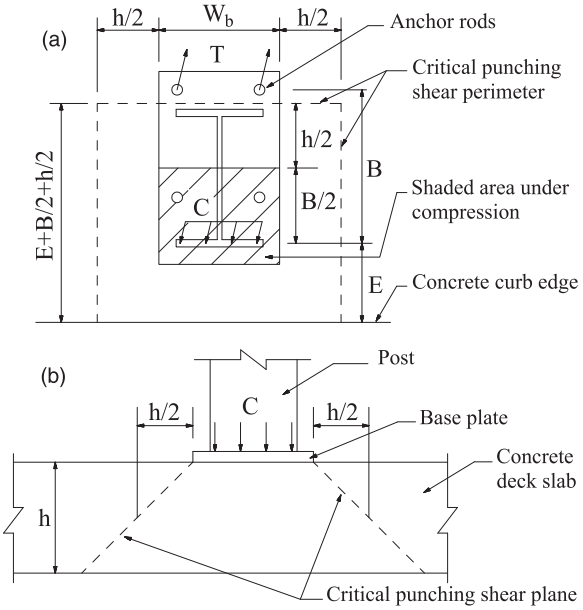

Fig. 2. Punching shear failure mode: (a) plan of punching shear plane; (b) section in punching shear plane (adapted from AASHTO 2012)

GFRP straight bars and bent bars have tensile strength of 1,100 and 700 MPa, respectively, and modulus of elasticity of 64 and 55 GPa, respectively.

Research Approach and Test Specimens

In bridge construction, as shown in Fig. 4, concrete deck slab is cast in place after the girders are placed over the abutments and piers. Then, the sidewalk is cast over the deck slab and exterior girder using dowels projecting from the slab. The steel posts and guardrails are then assembled. This research investigates the structural performance of the joint between the steel post of the bridge guardrail and the deck slab cantilever overhang. GFRP bent bars are used as stirrups for the curb under the post location, and the headed bars are used for bar anchorage to reinforce the deck slab cantilever-steel post joint, as well as the top reinforcement of the cantilever slab. The type of guardrail used in this study is PL-2. For PL-2 guardrails, the governing design load is usually a lateral static load of 100 kN·m, which is multiplied by 1.7 load factor as specified by the CSA (2006b). Hence, the total factored load to be resisted by the rail-post system is 170 kN·m. This

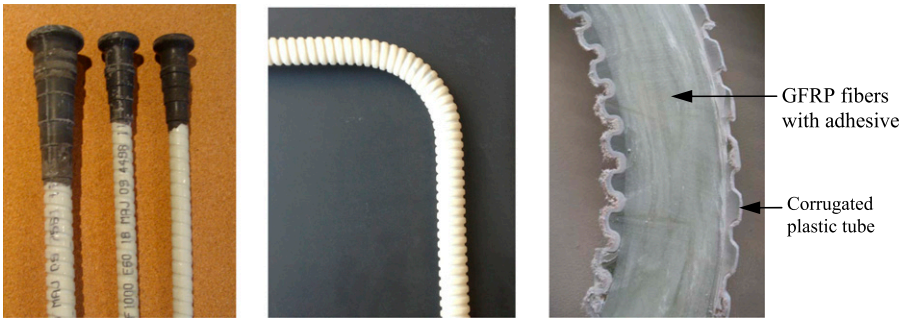

Fig. 3. Views of the GFRP bar types considered in this study: (a) headed bar; (b) bent bar; (c) a slice of the bent bar (images by Hossein Azimi and Khaled Sennah)

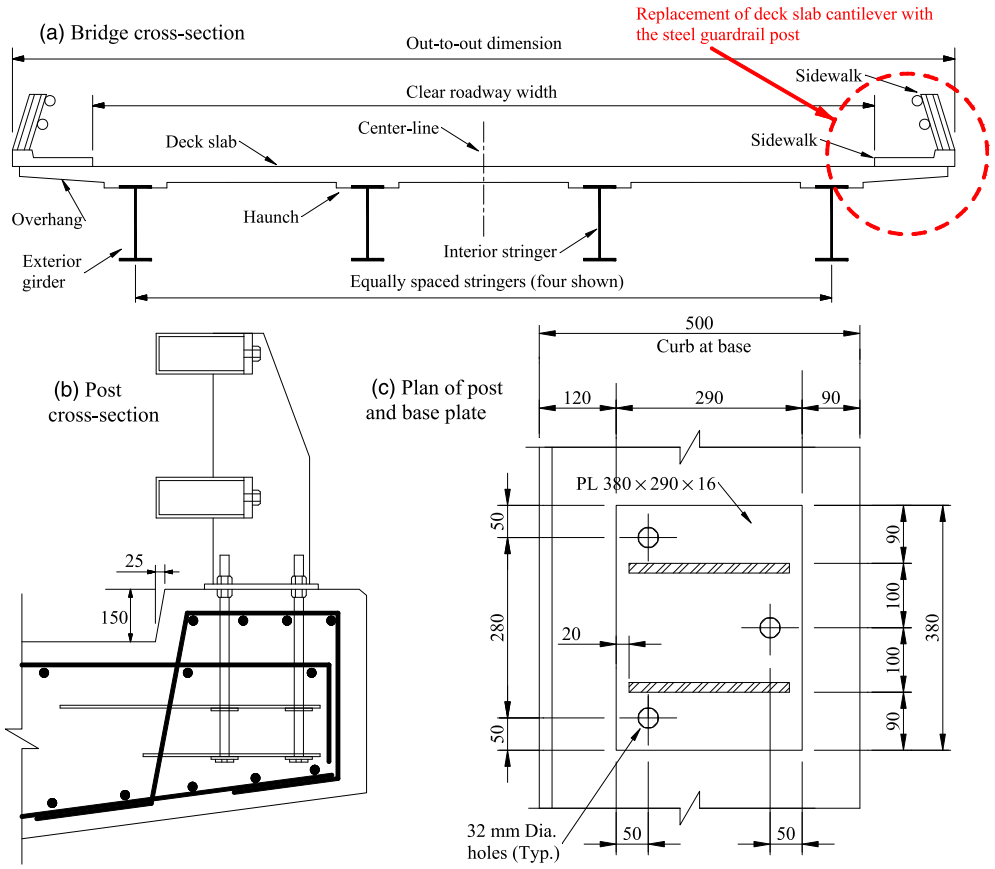

Fig. 4. Schematic diagram of post deck cantilever joint under consideration: (a) bridge cross section; (b) post cross section; (c) plant of post and base plate

load is to be distributed along 1.05 m of the guardrail and be applied at 790-mm height from the top surface of the deck slab, as specified by the CSA (2006b).

Four full-scale cantilever post specimens were erected and then tested to collapse at the structures laboratory of Ryerson University. Fig. 5 shows dimensions of the cantilever slab specimens. The first specimen in each set [designated as steel specimen 1 (SS1) and SS2] was a control specimen with the deck slab reinforced with steel bars of 400-MPa specified yield strength. The second specimen in each set [designated as GFRP specimen 1 (GS1) and GS2] was identical to the first one except that it was reinforced with GFRP straight and bent bars in addition to straight bars with headed ends. The slab cantilever was 2.5×2.5 m in plan, with the steel post mounted near the tip of the cantilever at the midwidth of the specimens.

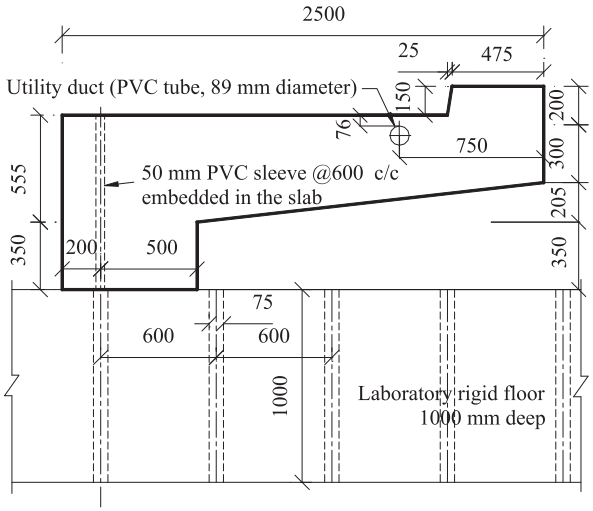

Fig. 5. Dimensioning of the specimen

Fig. 5 shows that there is a utility duct embedded in the slab at 750-mm distance from the outer face of the deck slab cantilever tip. This utility duct was made of 89-mm-diameter PVC tube. To facilitate applying horizontal load near the top of the steel post, the simulated fixed end of the deck slab cantilever was enlarged, and four 50-mm-diameter PVC sleeves were embedded in the enlarged end at 600-mm spacing, as shown in Fig. 5. These ducts were used to apply tie-down anchors to ensure full fixity of the deck slab cantilever end. Figs. 6(a and b) show the bar details of the steel-reinforced specimens and the GFRP-reinforced specimens, respectively.

Figs. 7(a and b) depict details and sizes of the steel post, base plate, anchor bolts, and anchorage system. Regular commercial steel with yield strength of 350 MPa was used in post and base plate. ASTM 354 BD fully threaded anchor bolts were used with the nominal diameter of 22 mm and specified tensile strength of 1,035 MPa. In addition, Fig. 7(c) shows a view of the fabricated steel plate assembly embedded in each specimen to provide anchorage for bolts as is the practice in the United States for steel post–curb detailing.

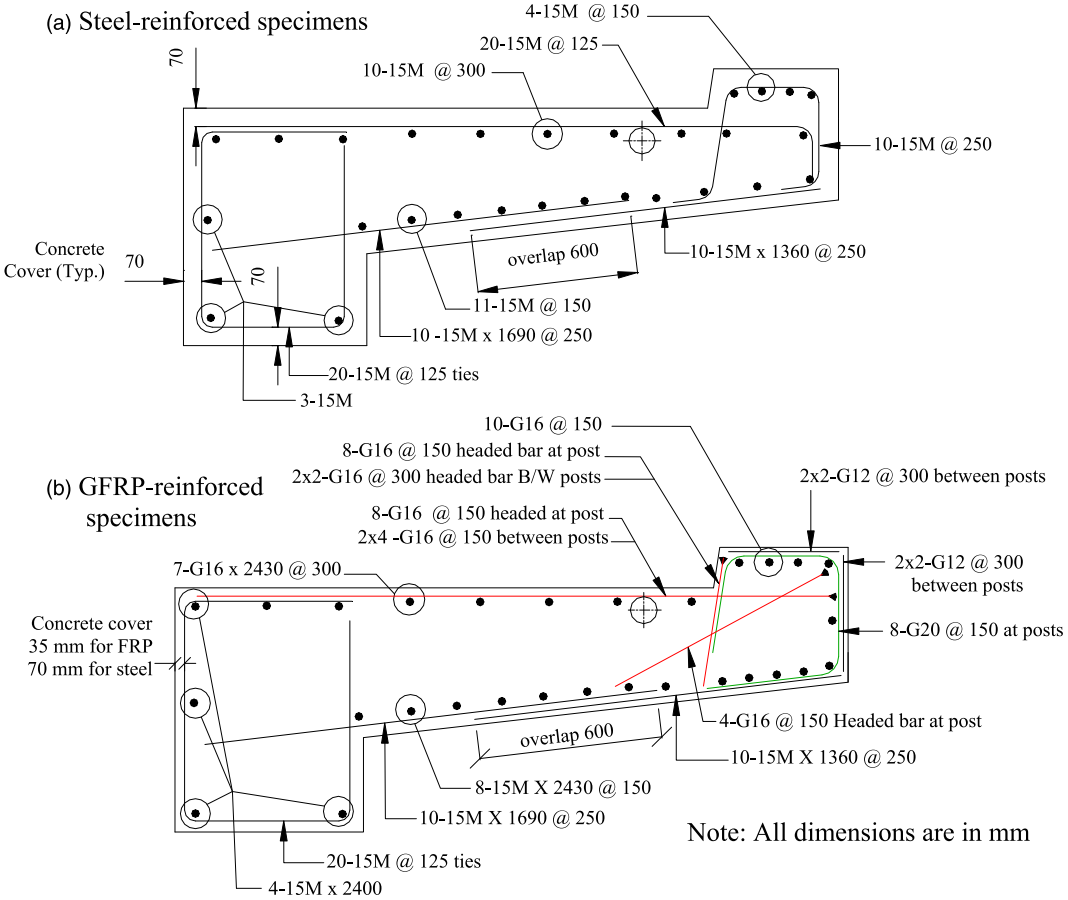

Fig. 6. Detailing of reinforcement: (a) steel-reinforced specimens; (b) GFRP-reinforced specimens

Structural steel for the steel plates in the anchorage assembly had a yield strength of 300 MPa. More details of the post anchorage assembly can be found elsewhere (Sennah et al. 2011b). Views of the reinforcement used at the post location of the steel-reinforced and GFRP-reinforced specimens are shown in Figs. 8(a and b).

Test Setup, Instrumentation, and Test Procedure

All specimens were fabricated in the structures laboratory. First, timber formwork was assembled. Then, reinforcing bars were assembled, followed by installation of the anchorage system and anchor bars. Concrete casting was performed using ready-mix concrete.

Fig. 9 shows a schematic diagram of the test setup. Four 44.45-mm-diameter (1.75-in.) all-threaded rods were inserted in the PVC embedded tubes at the enlarged end of the slab cantilever to tie the specimens to the laboratory strong floor. Steel hollow structural section (HSS) beams were fixed to the laboratory floor, and two hydraulic jacks, shown to the right of the enlarged end of the slab in Fig. 9, were used to prevent rigid body movement of the specimen when applying horizontal load on the steel post. The lateral load was applied to the steel post at 790 mm from the top surface of the concrete slab. LVDTs were installed at predetermined locations in the specimens as shown in Fig. 9 to record lateral and vertical displacement. These locations are (1) vertical deflection of the cantilever

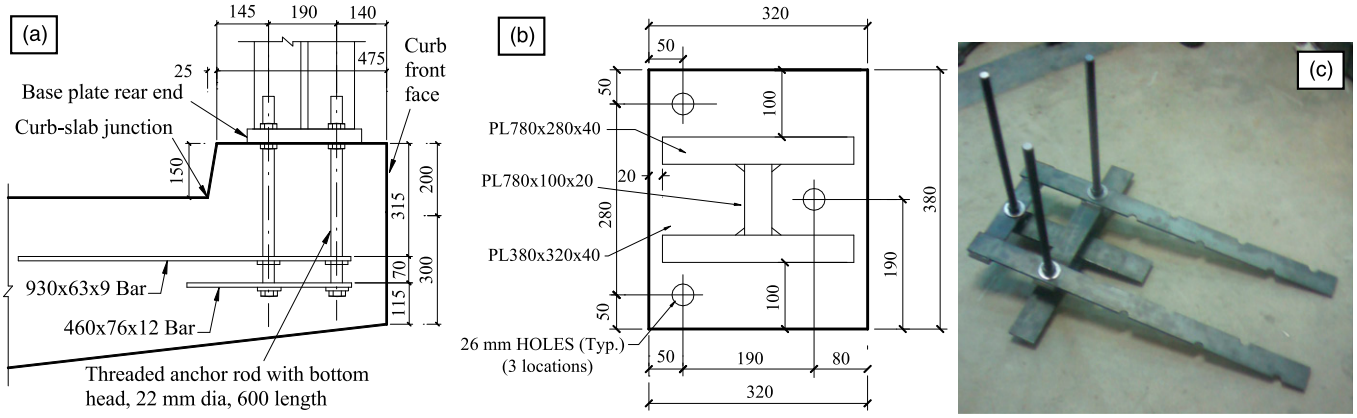

Fig. 7. Views of the fabricated post anchorage system (image by Navid Nikravan)

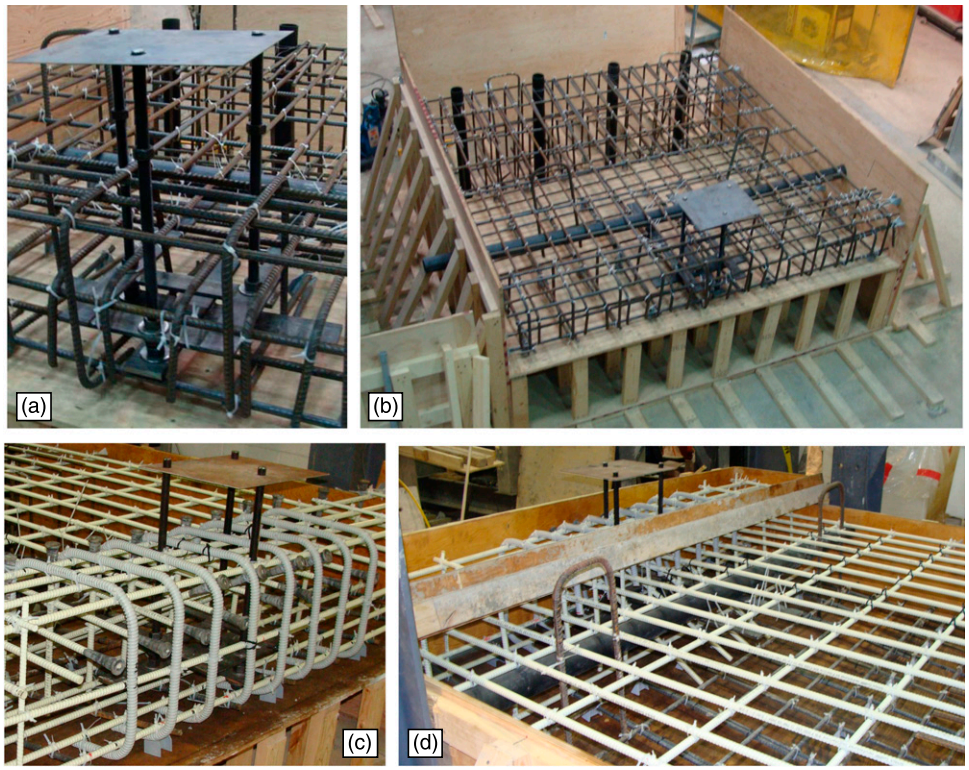

Fig. 8. Views of bar arrangement and formwork: (a) and (b) steel-reinforced specimens; (c) and (d) GFRP-reinforced specimens (images by Khaled Sennah, Navid Nikravan, and Jacob Louie)

tip, (2) horizontal deflection of the steel post at 790 mm from top surface of the concrete slab, (3) the uplift at the location of the tie-down system, (4) the rigid body movement of the specimens at the inner side of the enlarged portion of the deck slab, and (5) the horizontal displacement of the cantilever tip. Fig. 10 shows sample views of a specimen before testing. Visual inspection was conducted at each load increment during the test to record any change in structural integrity of the specimen and identify crack initiation and propagation. Failure of the specimen was considered reached when the specimen could not absorb more load.

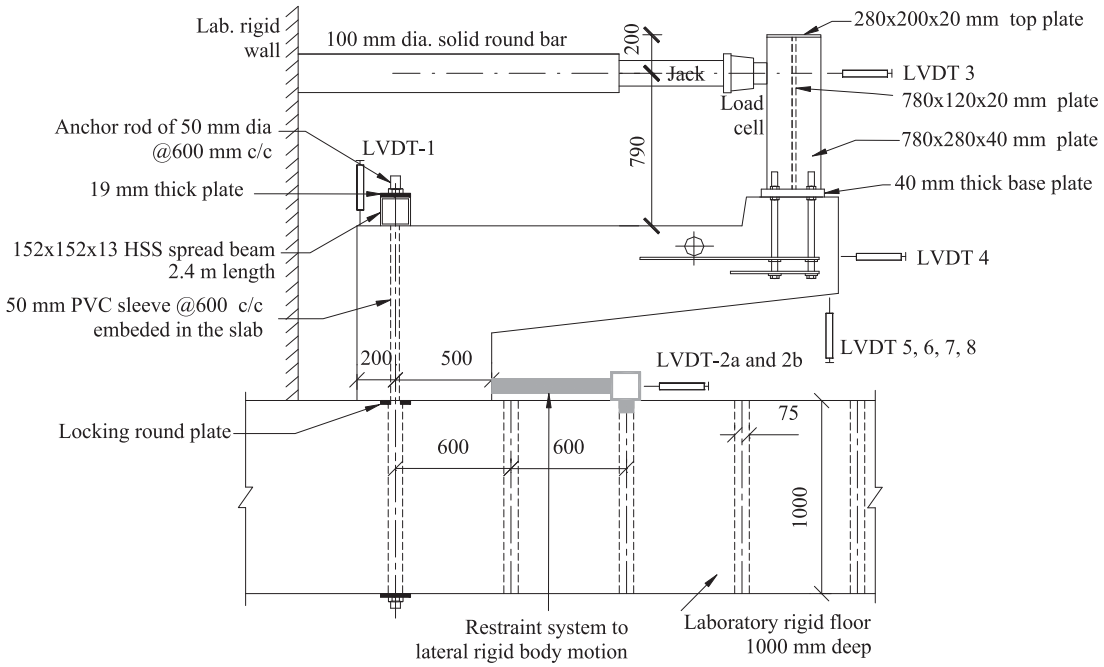

Fig. 9. Schematic diagram of the test setup

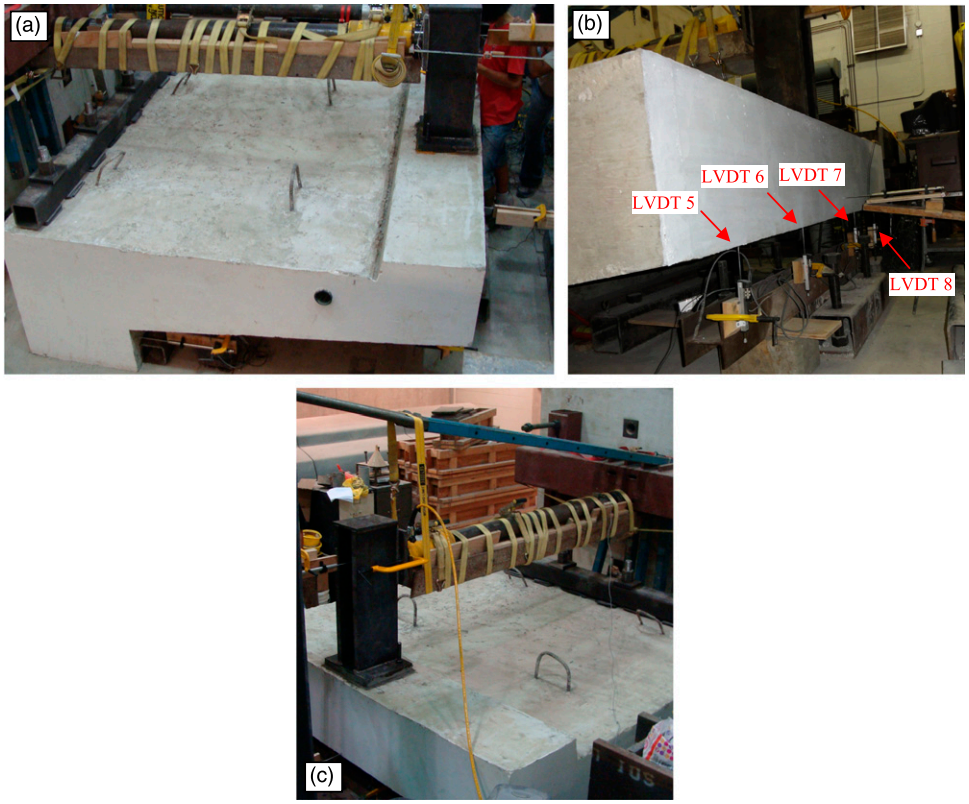

Fig. 10. Specimen view before testing: (a) side view; (b) LVDTs 5, 6, 7, and 8 installed under the curb; (c) front view (images by Khaled Sennah)

Test Results

Five concrete cylinders were tested in axial-compression to collapse at the time of testing of each specimen, and the characteristic strength of concrete was calculated in accordance with the CSA (2006a). As such, the characteristic strengths of concrete at the time of testing were 38.68 and 34.27 MPa for steel-reinforced specimens SS1 and SS2, respectively, and 33.54 and 32.87 MPa for GFRP-reinforced specimens GS1 and GS2. All experimental observations are summarized in Figs. 11(a–j), showing photos of the crack pattern along with the jacking loads at which these cracks first started or propagated for all four specimens. After each test, the cracked concrete cover was pushed out manually to further examine the failure region. Fig. 12 shows the rotation in the base plate of the post, and Fig. 13 illustrates the load–displacement relationship for all four specimens. In addition, important experimental results observed are tabulated in Table 1.

All specimens exhibited first crack starting near the rear corner of the base plate and propagating toward the front face of the slab curb at an angle following the torsion-shear crack pattern. Other minor cracks appeared at the rear end of the anchors that are in tension and the inner edge of the curb, as expected from the splitting forces in concrete resulting from pull-out of the anchors embedded in concrete. With increase in the applied load, cracks propagated toward the top tip of the front face of the slab curb and then to the side of the front face of the curb at higher load, as depicted in Fig. 11(a) for specimen SS1 as an example. Cracks were then widened with increase of applied load to the extent that the concrete cover to reinforcement along the front side of post base plate began to spall, as depicted in Fig. 11(b) for specimen SS1 as an example. No sign of

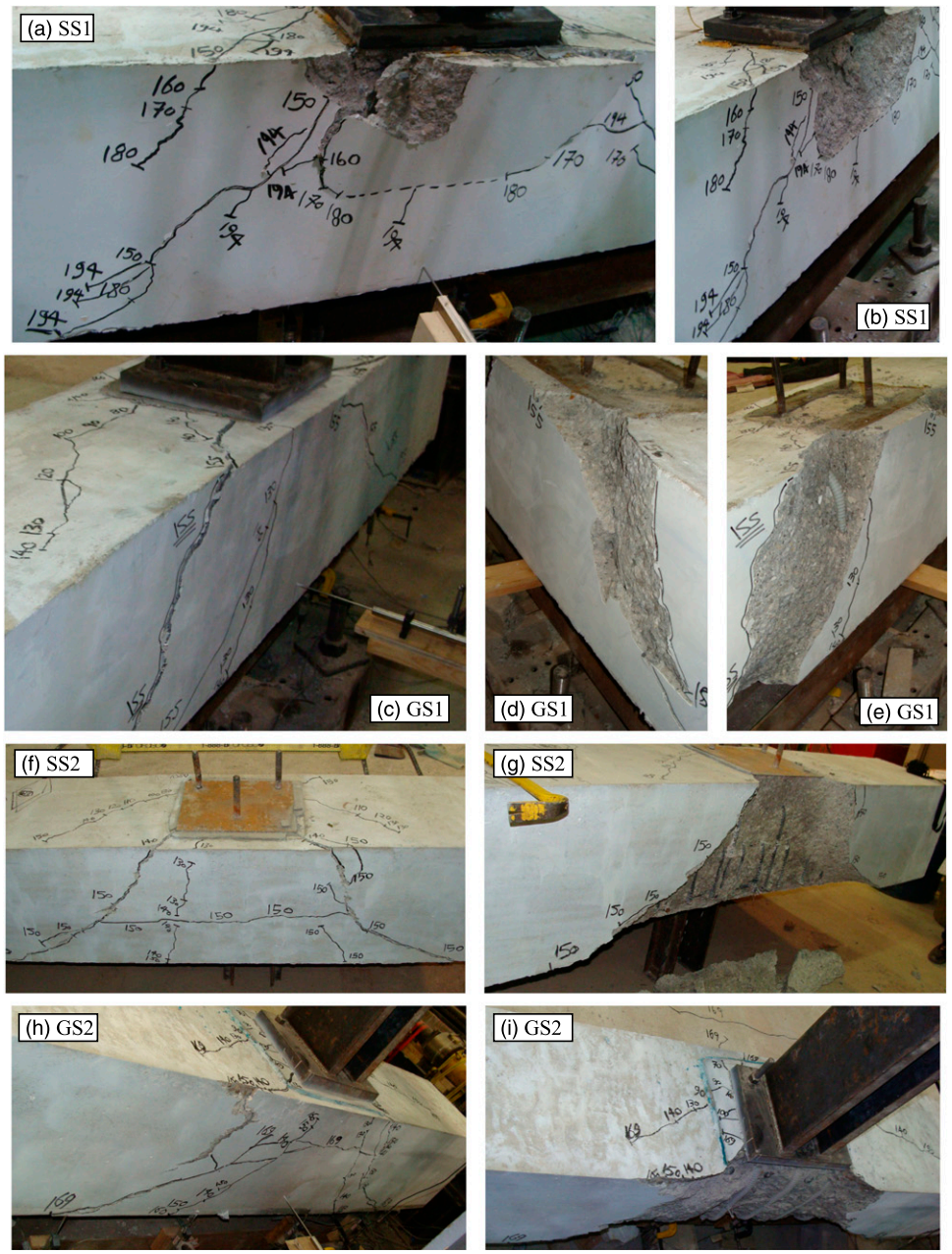

Fig. 11. Views of crack patterns at failure of the tested specimens (a) and (b) SS1; (c), (d), and (e) GS1; (f) and (g) SS2; and (h) and (i) GS2 (images by Khaled Sennah)

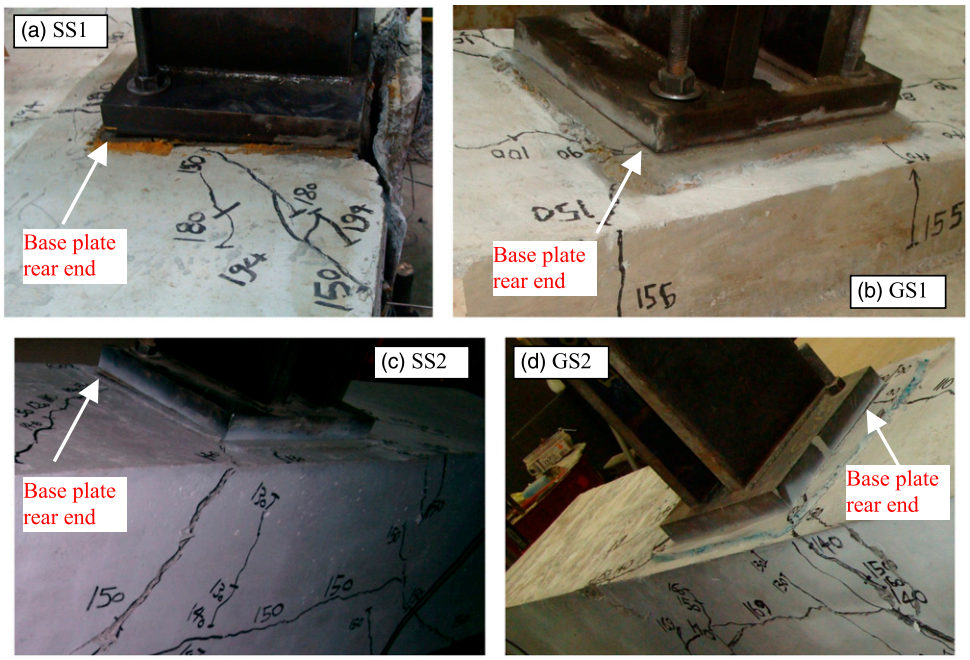

Fig. 12. Rotation of the base plate in all tested specimens: (a) SS1; (b) GS1; (c) SS2; (d) GS2

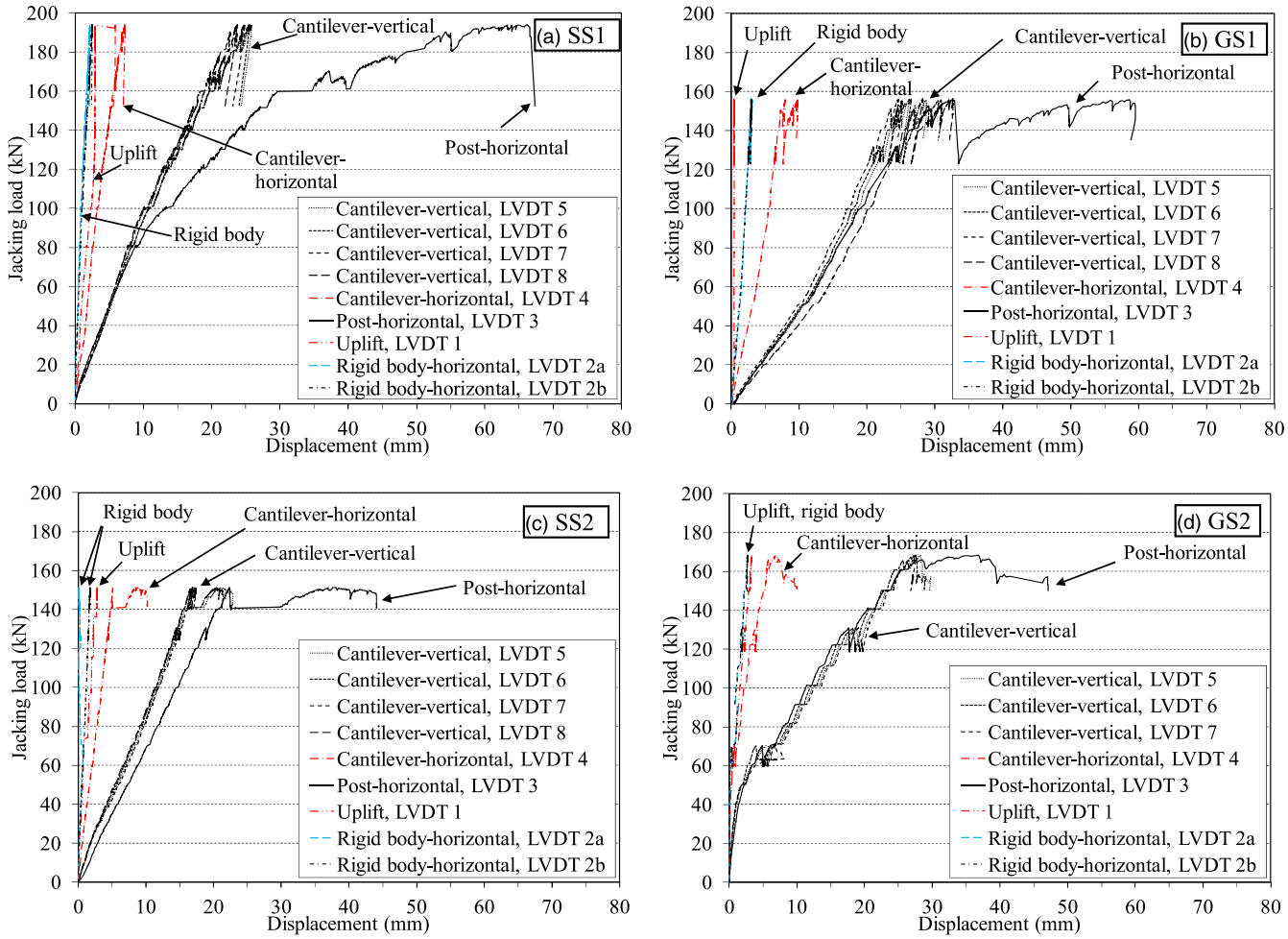

Fig. 13. Jacking load–displacement relationship for all specimens: (a) SS1; (b) GS1; (c) SS2; (d) GS2

Table 1. Experimental Ultimate Jacking Load and Displacements

Characteristic	SS1	GS1	SS2	GS2
f_c' (MPa)	38.68	33.54	34.27	32.87
Jacking load at first visible crack (kN·m)	150	80	80	90
Jacking load at first crack beyond the curb–slab junction (kN·m)	180	155	N/A	169
Specimen ultimate jacking load (kN·m)	194.7	156.4	151.8	169.1
Specimen maximum uplift (mm)	5.85	0.45	2.82	3.35
Cantilever maximum deflection (mm)	24.96	26.5	20.44	27.77
Specimen ultimate rigid body movement (mm)	2.36	2.97	0.94	1.89
Post maximum lateral deflection (mm)	64.47	32.63	37.88	36.12

Note: N/A = no visible flexural crack was observed.

failure in GFRP or steel reinforcement appeared after testing. However, steel stirrups in case of steel-reinforced specimens and GFRP bents and headed ends in case of GFRP-reinforced specimens were exposed after spalling of the concrete cover as depicted in Fig. 11(i) for specimen GS2.

Fig. 11 shows that the majority of the cracks were on the front side of the curb; however, few visible flexural cracks appeared beyond the slab–curb junction (i.e., on the deck slab cantilever portion) at the final stages of loading of each specimen except specimen SS2. These flexural cracks were recorded at 180, 155, and 169 kN·m for specimens SS1, GS1, and GS2, respectively, which are all very close to the final ultimate loads mentioned in Table 1. No indication of failure in the steel anchors was observed; however, steel anchors on the tension side appeared to be deformed in bending.

Figs. 13(a–d) depict the jacking load–displacement relationship for specimens SS1, GS1, SS2, and GS2, respectively, whereas Table 1 summarizes the recorded load and displacement at various stages of loading. It can be observed that the tie-down system as well as the horizontal restraint to the enlarged portion of the slab was effective in providing fixity, since comparatively small rigid body displacements were recorded. As for deflection of the post in each specimen, one may observe that they were very close to each other and generally maintained linear relationship with the applied load through a significant portion of the load-deflection history depicted in Fig. 13, given the enlarged sized of the post to prevent premature failure in flexure to divert specimen failure to be at the postcurb junction. However, the load-deflection relationships of the post changed to be nonlinear while approaching failure as a result of the deformation of the steel anchors in the tension side of the steel baseplate, as will be explained in the next section. It should be mentioned that the structural evaluation of the guardrail is considered as an extreme limit state (AASHTO 2012) controlled only by strength requirements not the displacements. Therefore, only the ultimate loads may be of interest. However, a guardrail system exhibiting higher flexibility may favor the energy absorption of the vehicle impact to the post, if not compromising safety criteria.

Discussion of Failure Modes

In general, base plates are classified as rigid or flexible, which is mainly controlled by the plate thickness. If the plate thickness is such that steel yielding does not occur under design loads, the plate is

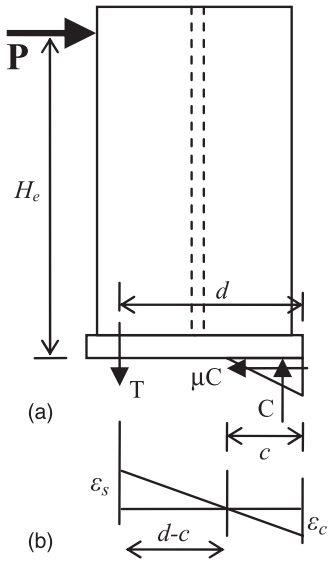

Fig. 14. Free-body diagram of the post

classified as rigid plate (Eligehausen et al. 2006). The type of analysis used to calculate load distribution under the plate is also subjected to the type of the plate. If rigid plates are used, elastic analysis is used and a linear strain distribution is assumed, resulting in a triangular concrete stress block. In the case of flexible plates, plastic analysis is used provided that the plate could exhibit sufficient ductility to enable load redistribution. In plastic analysis, it is assumed that all tension-loaded anchors sustain equal loads and there is a rectangular compressive stress block beneath the plate (Eligehausen et al. 2006).

Because a 40-mm-thick plate is considered in this study, it did not undergo any yielding as observed experimentally. Thus, the plate could be classified as rigid plate and therefore a linear strain distribution is assumed under the plate. Also in this study, there is no compressive force applied on the guardrail and only a lateral load is presented, applying a moment and shear at the base plate. With the application of elastic analysis and considering the fact that the bolt located on the compression side does not contribute in the analysis, tension and compression forces shown in Fig. 14 denoted by T and C, respectively, are obtained as

$$T = 2A_b E_s \varepsilon_s; \quad C = b\left(\frac{c}{2}\right) E_c \varepsilon_c \tag{2}$$

where A_b = cross-sectional area of one bolt in tension; E_s and E_c = elastic modulus of the steel and concrete, respectively; ε_s and ε_c = strain in steel and maximum strain in concrete, respectively; and b and c = width and depth, respectively, of the triangular compression block. Using the linear strain distribution and enforcing the equilibrium of the tension and compression forces (because there is no axial compression or tension on the post), c could be obtained using the following:

$$2A_b E_s (d - c) - 0.5 E_c b c^2 = 0 \tag{3}$$

This equation does not depend on the applied load or moment for this type of loading and post geometry. The definition of d in Eq. (3) is illustrated in Fig. 14 as the distance between the steel plate edge and the location of anchors in tension. In Eq. (3), the following values are considered for parameters used in this study: $E_s = 200$ GPa,

$A_b = 380$ mm^2, $d = 270$ mm, and $b = 380$ mm, and E_c is calculated using the following equation (CSA 2006a):

$$E_c = \left(3{,}000\sqrt{f_c'} + 6{,}900\right)(\gamma_c/2{,}300)^{1.5} \quad (4)$$

where γ_c = concrete density assumed as 2,400 kg/m^3. Considering concrete characteristic compressive strength tabulated in Table 1 for each specimen, E_c is obtained using Eq. (4) for each specimen. Consequently, c is calculated from Eq. (3) as 75.6, 77.2, 77.0, and 77.5 for specimens SS1, GS1, SS2, and GS2, respectively. Assuming a triangular compression block determined by elastic analysis and the geometry of the post shown in Fig. 14, the following relationship is written between C and P:

$$C = P\left(\frac{H_e}{d - c/3}\right) \quad (5)$$

where P = lateral applied load and H_e = vertical distance of the lateral load from the bottom of the base plate. For the studied specimens, $H_e = 640$ mm, and the ratio of the compression force C to the applied lateral load P is about 2.6 from Eq. (5) for all specimens.

If the base plate is subjected to shear and considerably large bending moment, the shear is entirely resisted by the friction force generated under the base plate in the concrete compression zone (Eligehausen et al. 2006). In cases where the compressive load is also applied, this assumption is more valid because a larger concrete area will be under compression. For the calculation of such friction forces, the static friction coefficient μ is used, which is multiplied by the total compression force under the base plate. Cook and Klingner (1989) suggested the application of a static friction coefficient of 0.43 where the base plate is in direct contact with concrete. However, DeWolf and Ricker (2003) suggested a coefficient of 0.7 be used. If concrete grout is used under the base plate, which is usually the case, DeWolf and Ricker recommended a coefficient of 0.55.

Because the ratio of the compression force C to the applied lateral load P is about 2.6, if all the shear at the base plate is resisted by the friction, therefore the minimum required friction coefficient is $\mu = 1/2.6 = 0.38$, which is less than the recommended values mentioned previously. Hence, this friction force could be generated under the base plate. This could be the case for specimens SS2 and SG2, where appropriate grouting was used under the base plate. A very similar failure mode between SS2 and SG2 shown in Figs. 11(g and i), respectively, acknowledges the similar stress distributions in such specimens. Therefore, the compression block under the base plate is subjected to large compressive and frictional shear stresses. The shear stresses are also intensified because of the shear stresses induced by the torque applied on the edge of the cantilever overhang generated from the lateral load. Hence, it could be concluded that the concrete edge around the base plate is under significant combined stresses, resulting in the failure of the unconfined concrete as depicted in Fig. 11(g) for steel-reinforced specimen SS2 and Fig. 11(i) for GFRP-reinforced specimen GS2. This type of failure occurred mainly because of insufficient edge distance of the guardrail fixture to the concrete. Similarly, Hite et al. (2008) observed concrete edge failure under the base plate of steel pedestals subjected to applied lateral and constant vertical loads because of the insufficient edge distance of postinstalled stud anchor bolts. Such local failure could not be detected without visual observations and was considered brittle because the recorded load-deflection history of the deck slab cantilever shown in Fig. 13 was generally linear until reaching the failure load.

If the base plate thickness is such that the plate is classified as flexible, then the lever arm (the arm between tensile forces in bolts and resultant of concrete compressive stress block) is smaller than the case of the rigid plate (Eligehausen et al. 2006), which means that the distance of the resultant compressive load to the concrete edge is more than that in case of rigid plate. Therefore, if a flexible plate is used, it is expected to have less compressive stresses applied on the unconfined concrete cover and probably a different mode of failure occurs, which could be a subject for further investigations.

Comparison of Experimental Ultimate Loads with Design Loads

With respect to the ultimate load-carrying capacity of the tested specimens shown in Table 1, it can be observed that failure loads were 194.68 and 151.76 kN·m for the steel-reinforced specimens SS1 and SS2, respectively, and 156.35 and 169.11 kN·m for GFRP-reinforced specimens GS1 and GS2. However, the authors believe that the results of the first set of specimens (i.e., SS1 and GS1) could have been affected by the irregular shape of the top surface of concrete in contact with the base plate of the post, because proper grouting was not applied on those specimens. As mentioned previously, the type of guardrail used in this study is PL-2, for which the total lateral design factored load is 170 kN·m distributed over a length of 1.05 m on the guardrail. Therefore, the lateral load applied at individual posts will be smaller than 170 kN·m given the continuity of the guardrail between posts that distributes the lateral load applied to the adjacent posts.

The AASHTO LRFD punching shear capacity of the curb under the post is also obtained for the tested specimens. According to dimensions of the post shown in Fig. 7 and Eqs. (1*a*)–(1*c*), $h = 500$, $B = 250$, $W_b = 380$, $E = 60$, and $d_b = 270$ mm and therefore the critical shear area is obtained as 750,000 mm^2. Because the concrete compressive strength is different in tested specimens, a different V_r is obtained for each specimen. In addition, according to Eq. (5) the ratio of the compression force under the post to the transverse load applied to the post is about 2.6. Therefore, the equivalent lateral load causing punching shear is obtained as shown in Table 2 for all specimens. Then, the factor of safety in design of postcurb junction is calculated as the ratio between the punching shear resisting force and the experimental ultimate jacking load. As depicted in Table 3, the factors of safety are all greater than one, confirming the experimental results, where no punching shear was observed.

Table 2. Comparison of Punching Shear Capacity with Experimental Loads

Characteristic	SS1	GS1	SS2	GS2
f_c' (MPa)	38.68	33.54	34.27	32.87
Experimental ultimate jacking load (kN·m)	194.7	156.4	151.8	169.1
Punching shear strength, v_c (MPa)	0.953	0.887	0.897	0.878
Punching shear resisting force, V_r (kN·m)	714.5	665.3	672.6	658.7
Equivalent lateral load causing punching shear (kN·m)	274.8	255.9	258.7	253.3
Factor of safety against AASHTO LRFD punching shear	1.41	1.64	1.70	1.50

Analysis of Postrail System Using FEM

To examine the load sharing between posts, finite-element analysis (FEA), use of *SAP2000* software was conducted followed by a simplified FEA modeling. According to the developed standards for guardrail systems (AASHTO 2012), the post consists of two vertical steel plates $664 \times 250 \times 16$ mm, spaced at 200 mm, and two rails. The rails have similar cross sections of HSS $203 \times 102 \times 10$ located at 680 and 330 mm above the base plate positioned on the strong axis against lateral load. The post and rail system was modeled by beam elements, whereas the deck overhang was modeled by shell elements with various thicknesses representing the tapered shape of the tested specimens. A general view of the FEA models is shown in Fig. 15(a).

Four different FEA models were generated with four spacings between posts, taken as 1.0, 1.5, 2.0, and 2.5 m. As the governing loading scenario for posts, a lateral load of 170 kN·m was applied at the middle post in each model, as depicted in Fig. 15(a), and the share of each post was obtained from the analysis and tabulated in Table 3. As expected, the share of the middle post, at the location of the lateral load, is quite high for large post spacing. The share of the adjacent posts increases when the post spacing decreases, as depicted in Fig. 15(b). It can be observed that the base shear of post No. 1 (middle post) decreases with an order higher than the linear rate with respect to the post spacing.

In addition to the analytical results obtained using *SAP2000*, a simplified FEA analysis was also undertaken to demonstrate the applicability of such a simplified method in post and rail systems. A similar simplified idealization was used by Matta and Nanni (2009) for open post concrete railings for nonlinear FEA analysis of post-rail systems. Assuming the rigidity of the deck overhang is much more than that in posts, one could take the base of post as fixed support. From the theoretical point of view, each post is under a share of the lateral load and will deform as a free cantilever under an applied lateral load. Therefore, each post could be idealized by a spring whose stiffness is obtained by

$$k_p = \frac{3E_pI_p}{H_e^3} \tag{6}$$

where E_pI_p = flexural rigidity of the post and H_e = height of the applied lateral load shown in Fig. 14. As such, the post-rail system may be simplified by the model shown in Fig. 16, in which degrees of freedom (DOF) are denoted by u_1 to u_4. Hence, the displacement vector is shown as

$$U = [u_1, u_2, u_3, u_4]_{4\times 1} \tag{7}$$

Fig. 16 shows only half of the system because of symmetry in the load and geometry. In addition, only three adjacent posts to the middle post are considered, since further posts receive almost no share from the applied lateral load. For such an idealized model, the system stiffness matrix is assembled as

$$K = \begin{bmatrix} k_{11} & k_{12} & 0 & 0 \\ & k_{22} & k_{23} & 0 \\ \text{Sym.} & & k_{33} & k_{34} \\ & & & k_{44} \end{bmatrix}_{4\times 4} \tag{8}$$

whose entries are

$$k_{11} = \frac{k_p}{2} + k_{rt} + k_{rb}\left(\frac{h}{H_e}\right)^3 \tag{9a}$$

$$k_{12} = k_{23} = k_{34} = -k_{rt} - k_{rb}\left(\frac{h}{H_e}\right)^3 \tag{9b}$$

$$k_{22} = k_{33} = k_{44} = 2k_{11} \tag{9c}$$

where h = height of the bottom rail from the base plate and parameters k_{rt} and k_{rb} = associated stiffness of the top and bottom rails, respectively, obtained as

$$k_{rt} = \frac{12E_rI_{rt}}{L^3}; \quad k_{rb} = (I_{rb}/I_{rt})k_{rt} \tag{10}$$

where I_{rt} and I_{rb} = moment of inertial of the top and bottom rails, respectively; E_r = modulus of elasticity of rails; and L = spacing between posts, as shown in Fig. 16.

It should be mentioned that k_{rb} is multiplied by $(h/H_e)^3$ assuming that the presence of the bottom rail has negligible effect on the lateral deformation of the post. This assumption is acceptable because of

Table 3. Shear at Base of Each Post for Various Spacing between Posts

Spacing between posts (m)							
2.5		2.0		1.5		1.0	
V_{base}	% of P	V_{base}	% of P	V_{base}	% of P	V_{base}	% of P
154.2	90.9	144.8	85.1	127.7	75.1	98.2	57.8
10.8	6.3	16.9	9.9	26.9	15.8	40.2	23.7
−3.4	−2.0	−4.7	−2.8	−5.6	−3.3	−1.4	−0.8
0.7	0.4	0.5	0.3	−0.3	−0.2	−2.7	−1.6
−0.3	−0.2	0.0	0.0	0.1	0.1	−0.3	−0.2

Note: P = applied lateral force (see Fig. 15); V_{base} = shear at base of the post (kN·m).

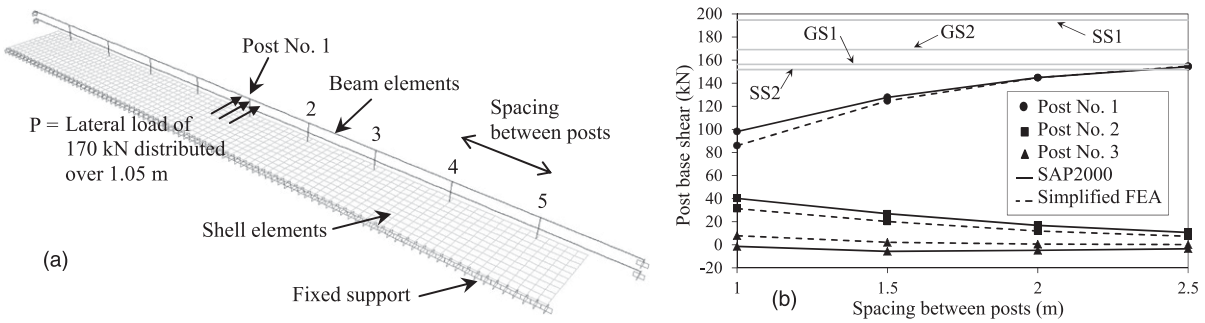

Fig. 15. Finite-element modeling: (a) details of the modeling; (b) results

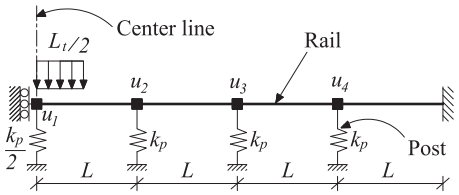

Fig. 16. Idealized post-rail model for simplified FEA analysis

the much higher post stiffness than that of the rail at that point for the guardrail system used in this study.

To find the solution of the guardrail system shown in Fig. 16, if F_0 is the fixed node solution, the displacement vector is obtained by $U = K^{-1}(-F_0)$, from which the force in the posts is obtained by $U \times k_p$. Results obtained from the simplified FEA analysis for four different post spacings are shown in Fig. 15(b) by dashed lines. It can be observed that results are close to those obtained by *SAP2000* for the middle post. However, the discrepancy increases with the reduction in post spacing because the assumptions are further affected for smaller post spacing. In conclusion, the simplified FEA method was able to capture results close to that obtained from FEA modeling using *SAP2000* for the studied rail post system in this paper.

For the sake of comparison, experimental ultimate loads are also included in Fig. 15(b), which are shown to be greater than those obtained analytically. Such results are presented as shear at post base for various post spacings as well as percentage sharing of applied lateral load among adjacent posts in Table 3. Therefore, it could be concluded that the tested specimens could be used with post spacing of 2.5 m or less.

Conclusions

According to experimental and analytical studies presented in this paper, the following conclusions are highlighted:

1. The minimum experimental lateral ultimate load was obtained as 151.8 kN·m, which may be considered sufficient to resist the share of the design lateral load received by each post of the guardrail system if the post spacing is smaller than 2.5 m. The GFRP-reinforced specimens proved to be as good as the steel-reinforced counterparts in structural design based on the ultimate load-carrying capacity reached experimentally.
2. The primary failure mode of the tested specimens was concrete breakout at outer side of the curb because of combined stresses at the unconfined concrete cover, which may be viewed as a premature type of failure. Signs of torsional cracks were present at the outer side of the curb during the loading history.
3. Lateral load sharing between posts of the guardrail system was studied by a linear FEA analysis for four different post spacings, namely 1.0, 1.5, 2.0, and 2.5 m. In addition, a simplified FEA analysis was also introduced whose results were close to the detailed FEA analysis. Results showed that the share of each post decreases with decrease in post spacing, though not linearly.
4. The AASHTO LRFD punching shear failure at the post–curb junction did not govern the design because the punching shear resistances of all tested specimens were greater than the applied experimental forces, with safety margins ranging from 1.4 to 1.7.

Acknowledgments

The writers of this report thank Schoeck Canada Inc. for supporting this research on the use of GFRP bars in bridge deck slabs. The authors thank Mr. Tony Wing, Transportation Chief Engineer of McCormick Rankin Corporation (MRC), for his valuable comments on GFRP bar arrangement and the experimental test setup. The authors sincerely acknowledge the support provided by Fonds Québécois de la Recherche sur la Nature et les Technologies in the form of a postdoctoral bursary to the first author and Ryerson University Scholarly Research and Creative Activity (SRC) fund.

References

AASHTO. (2009). *AASHTO-LRFD bridge design guide specifications for GFRP-reinforced concrete bridge decks and traffic railings*, Washington, DC.

AASHTO. (2012). *AASHTO-LRFD bridge design specifications*, 6th Ed., Washington, DC.

Ahmed, E., Matta, F., and Benmokrane, B. (2013). "Steel post-and-beam barrier with GFRP-reinforced concrete curb and bridge deck connection." *J. Bridge Eng.*, 10.1061/(ASCE)BE.1943-5592.0000470, 1189–1197.

American Concrete Institute (ACI). (2011). *Building code requirements for structural concrete (ACI 318M-11) and commentary*, Farmington Hills, MI.

Canadian Standards Association (CSA). (2004). "Design of concrete structures." *CSA standard A23.3-04,* Mississauga, ON, Canada.

Canadian Standards Association (CSA). (2006a). "Canadian highway bridge design code (CHBDC)." *CAN/CSA-S6-06,* Toronto.

Canadian Standards Association (CSA). (2006b). "Commentary on CAN/CSA-S6-10, Canadian highway bridge design code (CHBDC)." *CAN/CSA-S6.1-06,* Toronto.

Cook, R. A., and Klingner, R. E. (1989). "Behavior and design of ductile multiple anchor steel to concrete connections." *Rep. No. CTR 1126-3*, Univ. of Texas at Austin, Austin, TX.

DeWolf, J. T., and Ricker, D. T. (2003). *Column base plates, steel design guide series no. 1*, AISC, Chicago.

El-Gamal, S., Tobbi, H., El-Sayed, A., and Benmokrane, B. (2007). "Impact testing of concrete bridge barriers reinforced with new GFRP bars (types 201 and 301)." *Technical Rep.*, Univ. of Sherbrooke, Sherbrooke, QC, Canada, 84.

Eligehausen, R., Mallee, R., and Silva, J. (2006). *Anchorage in concrete construction*, Ernst & Sohn, Berlin.

Hite, M., DesRoches, R., and Leon, R. T. (2008). "Full-scale tests of bridge steel pedestals." *J. Bridge Eng.*, 10.1061/(ASCE)1084-0702(2008)13:5(483), 483–491.

Matta, F., and Nanni, A. (2009). "Connection of concrete railing post and bridge deck with internal FRP reinforcement." *J. Bridge Eng.*, 10.1061/(ASCE)1084-0702(2009)14:1(66), 66–76.

SAP2000 [Computer software]. Berkeley, CA, Computers and Structures.

Schoeck Canada Inc. (2013). "Schöck ComBAR technical information." ⟨http://www.contechaccessories.com/attachments/combar_technical.pdf⟩ (Jun. 25, 2013).

Sennah, K., Juette, B., Weber, A., and Witt, C. (2011a). "Vehicle crash testing of a GFRP-reinforced PL-3 concrete bridge barrier." *Proc., 4th International Conf. on Durability & Sustainability of Fiber Reinforced Polymer Composites for Construction and Rehabilitation*, Univ. of Sherbrooke, Sherbrooke, QC, Canada, 417–424.

Sennah, K., Nikravan, N., Louie, J., Hassaan, A., and El-Sayed, M., Al-Bayati, N. (2011b). "Experimental study on bridge deck-guard rail anchorage incorporating both GFRP bent bars and GFRP with headed studs." *Report prepared for Shoeck Canada Inc.*, Kitchener, ON, Canada.